Geophysical Research Letters

RESEARCH LETTER
10.1029/2020GL088030

Key Points:
- Ice cloud fraction is primarily determined by temperature, with substantial influence of dust extinction coefficient at about 250 K
- The larger dust extinction coefficient is, the larger ice cloud fraction is in the same temperature range by higher freezing chances
- The variation of ice cloud fraction is the highest at dust extinction coefficient of about 0.03 $km^{-1}$and temperature of about 250 K

Correspondence to:
K. Kawamoto,
kazukawa@nagasaki-u.ac.jp

Citation:
Kawamoto, K., Yamauchi, A., Suzuki, K., Okamoto, H., & Li, J. (2020). Effect of dust load on the cloud top ice-water partitioning over northern middle to high latitudes with CALIPSO products. *Geophysical Research Letters*, *46*, e2020GL088030. https://doi.org/10.1029/2020GL088030

Received 18 MAR 2020
Accepted 17 JUL 2020
Accepted article online 29 JUL 2020

Effect of Dust Load on the Cloud Top Ice-Water Partitioning Over Northern Middle to High Latitudes With CALIPSO Products

Kazuaki Kawamoto[1], Akira Yamauchi[2], Kentaroh Suzuki[2], Hajime Okamoto[3], and Jiming Li[4]

[1]Graduate School of Fisheries and Environmental Sciences, Nagasaki University, Nagasaki, Japan, [2]Atmosphere and Ocean Research Institute, The University of Tokyo, Chiba, Japan, [3]Research Institute for Applied Mechanics, Kyushu University, Fukuoka, Japan, [4]Key Laboratory for Semi-Arid Climate Change of the Ministry of Education, College of Atmospheric Sciences, Lanzhou University, Lanzhou, China

Abstract We quantified effects of dust load on the cloud top ice cloud fraction (ICF) in terms of the dust extinction coefficient (σ_{ext}). We analyzed 3-year data sets obtained from an active satellite sensor over middle to high latitudes in the northern hemisphere for temperatures (T) between 230 and 273 K and σ_{ext} values between 0.005 and 0.145 km^{-1}. At about 250 K, ICF changed by about 30% in response to the above range of σ_{ext}, whereas at extreme T values, ICF was relatively insensitive to σ_{ext}. Thus, we concluded that ICF was primarily determined by T, with substantial influence of σ_{ext} at about 250 K, likely due to increased opportunities for freezing as σ_{ext} increases. Sensitivity of ICF was the lowest both at the largest σ_{ext} and lowest T and at the smallest σ_{ext} and highest T, while it was the highest at about 0.03 km^{-1} of σ_{ext} and about 250 K.

Plain Language Summary If there are any physical parameters that influence the ICF except temperature (T), how much does this parameter influence ICF in a given T? Dust particles have been long known as efficient ice nucleating particles. Although previous studies suggested that more dust particles increased ICF, they did not use quantitative parameters of the dust amount, but less-quantitative indicators such as relative dust frequency. Therefore, we used the dust extinction coefficient (σ_{ext}) as a quantitative parameter of dust amount and examined the relationship between the dust amount and ICF for T between 230 and 273 K. We observed the following phenomena from satellite data. At about 250 K, ICF substantially depended on σ_{ext} likely due to increased opportunities for freezing as σ_{ext} increases. However, at extreme T values, ICF was relatively insensitive to σ_{ext}. Moreover, we found that sensitivity of ICF was the lowest both at the largest σ_{ext} and lowest T and at the smallest σ_{ext} and highest T, while it was the highest at about 0.03 km^{-1} of σ_{ext} and about 250 K. These behaviors of the ICF sensitivity could be understood from characteristics of T (the lower, the easier for freezing) and σ_{ext} (the larger, the easier for freezing).

1. Introduction

The Earth's clouds can consist of liquid droplets, ice crystals, or a mixture of both in the temperature range between approximately 235 and 273 K. Information on cloud thermodynamic phases (ice or liquid water, hereafter the cloud phase) is crucial for determining cloud radiative properties (Fu & Liou, 1993; Slingo, 1989). Liquid water droplets do not freeze instantaneously at 273 K. Liquid water droplets' freezing can be caused by aerosols acting as ice nucleating particles (INP) or may occur without INP below about 235 K (Pruppacher & Klett, 1978). The former, called as heterogeneous freezing, can be classified into contact, condensation/immersion, and deposition nucleation modes depending on the physical processes involved, and the latter is called as homogeneous freezing.

Dust particles blown into the atmosphere from arid and semiarid areas have long been recognized as a dominant INP in nature (Hoose & Möhler, 2012; Isono et al., 1959; Murray et al., 2012; Pratt et al., 2009; Sassen et al., 2003), and the importance of oceanic biological aerosols as INP has been pointed out in the Southern, North Pacific, and North Atlantic Oceans (Burrows et al., 2013; Wilson et al., 2015). Recently, Tobo et al. (2019) found that dust particles from the arctic land surface had remarkably high ice-nucleating ability, which could influence mixed-phase clouds in the Arctic, where this type of cloud prevails (Shupe et al., 2008).

Previous studies have demonstrated a bias in the temperature (T) dependence of cloud phase partitioning in climate models (Komurcu et al., 2014; McCoy et al., 2015). Thus, climate models cannot reproduce the radiative contribution of supercooled liquid clouds due to inappropriate cloud treatment compared with observations (Bodas-Salcedo et al., 2016). Tan and Storelvmo (2019) also emphasize the importance of realistic representations of the processes in mixed-phase clouds, particularly in the Arctic.

Observational studies of the cloud phase also have been conducted, mainly using the Cloud-Aerosol Lidar with Orthogonal Polarization (CALIOP) instrument aboard the Cloud-Aerosol Lidar and Infrared Pathfinder Satellite Observation (CALIPSO) mission, launched in 2006 (Hu et al., 2009; Yoshida et al., 2010). Ice cloud fraction relative to water clouds showed strong dependence on temperature and latitude (Yoshida et al., 2010). Figure 1b of Choi et al. (2010) presented a figure of CALIPSO-derived supercooled cloud fractions (SCF) (Hu et al., 2009) in several locations where dust loads would differ as a function of the cloud temperature, including Asia, South and North America, and Antarctica. They reported different SCF values, even for the same temperature, and suggested that enhanced glaciation by dust would influence the difference, demonstrating a negative correlation between SCF and the relative dust frequency used as an indicator of dustiness (also derived from CALIPSO data) at the −20°C isotherm. Kanitz et al. (2011) plotted a relationship between the fractions of ice-containing clouds and temperature using many lidar measurements from the ground (Chile, South Africa, and Germany) and a ship, and they attributed the ice fraction difference to variation in the aerosol condition, such as through anthropogenic pollution, mineral dust, forest fire smoke, and terrestrial biological material. Furthermore, Tan et al. (2014) adopted a method similar to that of Choi et al. (2010) using CALIPSO data and showed that SCF could be influenced by the existence of aerosols, comparing SCF with the relative aerosol frequencies of dust, polluted dust, and smoke aerosols on a global scale. Zhang et al. (2015) obtained a result similar to that of Tan et al. (2014), focusing on East Asia. These studies supported the suggestion that dust promotes freezing, but they had difficulty establishing quantitative relationships between the cloud phase fraction and INP properties, mainly because they used only aerosol-type information as an INP load indicator, which was converted into a less-quantitative parameter such as the relative dust frequency. Although Zhao et al. (2018) combined passive Moderate-resolution Imaging Spectroradiometer (MODIS) remote sensing data with active CALIPSO data and showed an increase in the ice cloud fraction with layered aerosol optical depth, the relationship between the ice cloud fraction and temperature remains unclear.

Recently, high latitudes and polar regions have drawn attention due to related phenomena, such as Arctic amplification (Screen & Simmonds, 2010; Taylor et al., 2013). This area is sensitive to warming through, e.g., via sea ice-albedo feedback (Manabe & Wetherald, 1975). This is a positive feedback that strengthens the initial warming by decreasing the Earth's reflectivity due to melting sea ice. Based on this situation, this study examined the quantitative effect of dust load on cloud top phase partitioning over middle to high latitudes in the Northern Hemisphere, where the climatic influence is important. This study adopted the dust extinction coefficient, which was retrieved from CALIPSO data by Nishizawa et al. (2011), which was based on Nishizawa et al. (2007, 2008), as the dust load indicator.

This paper is organized as follows. Section 2 describes the data and methods used. Section 3 presents and discusses the obtained results. Finally, section 4 summarizes our findings and gives future perspectives on this topic.

2. Data and Method

This section first describes the data sets used in this study. The products of the dust extinction coefficient at 532 nm (hereafter σ_{ext}), the cloud phase, and temperature (hereafter T) were obtained from the EarthCARE Research Product Monitor. The vertical and horizontal resolutions of all data sets averaged 240 m and 1.1 km, respectively. This system distributes the aerosol and cloud data derived from “A-train” constellation satellite data, e.g., CloudSat, CALIPSO, and Aqua, and is released to maximize the outcomes of the algorithm development activities using A-train data and prepared for the distribution of the JAXA EarthCARE products before launch.

First, a cloud and aerosol discrimination scheme (Hagihara et al., 2010) was developed to investigate relationships between clouds and aerosols. A cloud mask scheme was developed and validated using data obtained by ship-based lidar and 94-GHz radar in the midlatitudes (Okamoto et al., 2007) and tropical

western Pacific Ocean (Okamoto et al., 2008), and applied to CALIPSO and CloudSat data (KU-mask product).

After cloud signals were removed, an algorithm developed by Nishizawa et al. (2011) was applied to derive the extinction for three aerosol types. The algorithm simultaneously utilizes attenuated backscattering coefficient at 532 and 1,064 nm with depolarization ratio at 532 nm of CALIPSO data to retrieve the vertical profiles of the extinction coefficients at 532 nm for three types of aerosol, i.e., water soluble (a mixture of sulfate, nitrate, and organic aerosols), dust, and sea salt together with the difference in their optical properties. For the dust model, the following microphysical and optical properties were assumed: spheroidal shape; mode radius 2 μm, standard deviation 2.2 μm; log-normal size distribution; real and imaginary parts of the refractive indices at 532 and 1,064 nm of 1.51 and 3.4×10^{-3} and 1.50 and 2.5×10^{-3}, respectively; lidar ratio, defined as extinction coefficient to backscattering coefficient, at 532 nm of 48 sr; and depolarization ratio at 532 nm of 30%. This method considers nonsphericity and models the dust optical properties assuming a spheroidal shape (Dubovik et al., 2006). This introduction of nonsphericity in spheroids enabled us to model lidar ratio of 48 sr and depolarization of 30% with realistic values and to retrieve fraction and extinction coefficient of each spherical type in one grid box. The lidar ratio of dust assumed in this study is close to the measured values by Raman lidar (Müller et al., 2007). For more details on the retrieval algorithm and σ_{ext} product, see Nishizawa et al. (2011). As for the fixed lidar ratio assumed in this study, Wandinger et al. (2010) pointed out that Saharan dust cases could introduce 10–40% underestimation of σ_{ext} due to multiple scattering compared to CALIPSO products. Similar underestimation may be expected in the analyses of dust extinction when optical thickness becomes large. A fast method is needed to estimate the effects of multiple scattering on both backscattering coefficient and depolarization ratio to correct these effects. For the purposes, application of physical model and vectorized physical model developed for the interpretation of space-borne lidar seems to be promising (Sato et al., 2018, 2019).

For the cloud phase, an algorithm by Yoshida et al. (2010) was applied to clouds detected by the cloud mask scheme using CALIPSO data to determine the cloud particle phase and orientation of ice clouds. The algorithm uses the depolarization ratio and the ratio of attenuated backscattering coefficients for two vertically consecutive layers, with the modification by Hirakata et al. (2014). This modified method can discriminate the following seven cloud particle types: warm water (liquid droplets with $T \geq 273$ K), supercooled water (liquid droplets with $T < 273$ K), three-dimensional (3-D) ice (randomly oriented ice crystals), two-dimensional (2-D) plates (likely ice crystals containing horizontally oriented plates with specular reflection, liquid droplets, or randomly oriented ice crystals), a mixture of 3-D ice and 2-D plates, unknown1 (likely ice crystals containing horizontally oriented plates with weak specular reflection), and unknown2 (liquid droplets or randomly oriented ice crystals). We are particularly interested in liquid/ice partitioning and use warm water and supercooled water as liquid and use 3-D ice, 2-D plate, and a mixture of 3-D ice and 2-D plate as ice. Unknown1 and 2 were excluded from the analysis. For more details of the retrieval algorithm and cloud particle type product (KU-type product), see Yoshida et al. (2010) and Hirakata et al. (2014). These aerosol and cloud products, which were derived with the same CALIOP instrument, are completely coincident spatiotemporally.

For the meteorology, temperature information for every 240 m was taken from the European Center for Medium-range Weather Forecasts (ECMWF) Ancillary Atmospheric State Product, originally from the CloudSat products of CloudSat ECMWF-AUX R04 (Partain, 2007), to adjust the CALIPSO footprint.

The target period is 3 years from December 2006 to November 2009, and the target area is middle to high latitudes of greater than 45° in the Northern Hemisphere. As described above, the algorithm of Nishizawa et al. (2011) can also retrieve the extinction coefficients of water-soluble and sea salt aerosols. Although a mixture of more than one aerosol component in a single layer is frequently observed, the analyzed samples were limited to the portion of dust extinction coefficient larger than 70% of the total (three types of aerosols) extinction coefficient. This threshold of 70% was determined in view of both extracting the effect of dust on freezing and obtaining the enough number of samples. As a specific analysis method, we use the following comparison procedure. First, two consecutive layers (one layer is 240 m thick) are sought such that the upper layer is dominated by dust and the lower layer is classified as cloudy. This procedure is used in an effort to realize the assumption that the partitioning of the cloud phase is influenced by the aerosol of the closest layer in the context of using a lidar instrument. Lidar signals are easily attenuated by even thin cloud layers;

Table 1
Ranges of Each bin of T and σ_{ext}

	T (K)		σ_{ext} (1/km)	
1	230	237	0.005	0.009
2	237	244	0.009	0.015
3	244	251	0.015	0.027
4	252	259	0.027	0.047
5	259	266	0.047	0.083
6	266	273	0.083	0.145

therefore, the situation analyzed is mostly realized for a dusty layer just above the cloud top. Second, the ice cloud fraction (ICF hereafter) is calculated as the ratio of the ice sample number to the total (ice plus liquid water) sample number at each grid of T and σ_{ext} bins for the aforementioned temporal and spatial ranges. The analyzed ranges of T and σ_{ext} were taken for 230–273 K and 0.005–0.145 km^{-1}, respectively. Six bins were taken for both T and σ_{ext} as defined in Table 1.

Note that ICF in this study is not exactly the same as that referred to in numerical models, such as the fraction of ice crystals to total particles throughout the cloud layer or the fraction of frozen layers to all cloud layers, because lidar signals quickly attenuate in thick media. Rather, ICF can be interpreted as the frozen probability; this should be kept in mind when comparing the results of this study with model outputs.

3. Results and Discussion

3.1. Relationships Between ICF and T With Different σ_{ext}

Figure 1a shows the relationship between ICF and T with six σ_{ext} bins. ICF is a monotonic function of T for all σ_{ext} bins. The overall tendency of the graph is consistent with the findings of Choi et al. (2010), which showed the following in the SCF in their Figure 1: ICF values are generally about 30%, 55%, and 85% at approximately 260, 250, and 240 K, respectively; and flatter and steeper parts can be observed near the lowest and highest T range (especially near the lowest T in this study), and except these two ends, respectively. This feature suggests that the curves are convex in lower T, and they are concave in higher T ranges.

Note that the larger σ_{ext} is, the larger ICF becomes in the same T bin. Although the variation in ICF due to different values of σ_{ext} in the same T bin is smaller in bins near the low and high ends, that in intermediate T bins is larger. Hereafter, intermediate T and intermediate σ_{ext} mean about 250 K and about 0.03 km^{-1}, respectively. In particular, ICF values are most spread at the intermediate T range, with an almost 30% difference between the smallest and largest σ_{ext} values. In this temperature range, heterogeneous nucleation such as immersion freezing and condensation nucleation modes would be effective (Hoose & Möhler, 2012). It would be interesting to point out that ICF highly depends on σ_{ext} at the intermediate T range, but ICF is insensitive to σ_{ext} at the low and high ends of the T range.

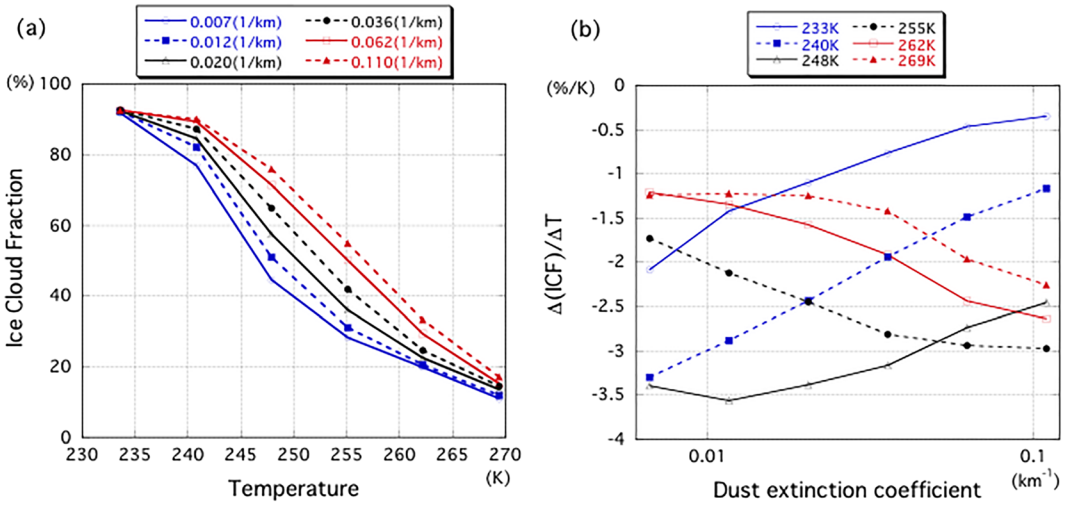

Figure 1. (a) Relationship between ICF and T with six σ_{ext} bins. The values of T and σ_{ext} cover from 230 to 273 K and from 0.005 to 0.145 (km^{-1}), respectively. (b) Sensitivity of ICF with regard to T as a function of σ_{ext}. Conditions of T and σ_{ext} are the same as those of (a).

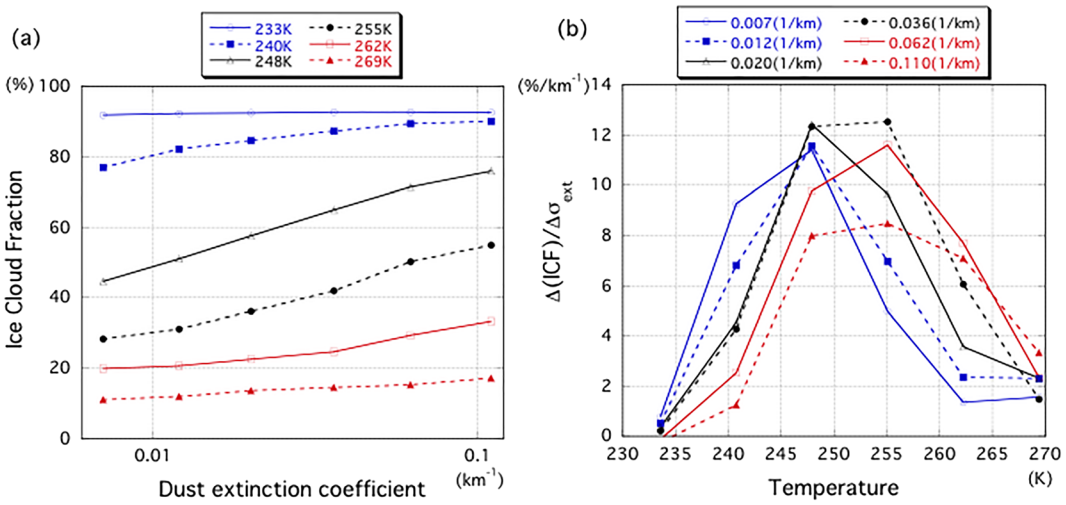

Figure 2. (a) Relationship between ICF and σ_{ext} with six T bins. (b) Sensitivity of ICF with regard to σ_{ext} as a function of T. conditions of T and σ_{ext} are the same as those of Figure 1a.

In order to further investigate the sensitivity of ICF with regard to T, we plot $\Delta\ (ICF)/\Delta T$, i.e., the slope in curves of Figure 1a, as a function of σ_{ext} for six T bins in Figure 1b. All values are negative, because ICF is a decreasing function of T, with three lower (233, 240, and 248 K) and three higher T ranges (255, 262, and 269 K) producing increasing and decreasing trends, respectively. These trends reflect convex shapes in lower T values and concave shapes in higher T values of Figure 1a, with an inflection point at the leftmost part (a weak decreasing trend) of the 248 K curve. In the lower T range, the magnitude of the sensitivity of ICF with regard to T increases as T increases, whereas in the higher T range, it decreases as T increases. This trend can be explained by the dominance of homogeneous nucleation processes at lower T, whereas higher T values approach the melting temperature. Moreover, we notice the following features: the highest sensitivity occurs at intermediate σ_{ext} and T values; the lowest sensitivity occurs at the highest σ_{ext} and lowest T values, and vice versa (especially at the highest σ_{ext} and lowest T case in this study); the higher sensitivity occurs at smaller σ_{ext} in the lowest T, and vice versa. These features on the sensitivity of ICF will be understood in the next subsection together with the sensitivity of ICF with regard to σ_{ext}.

3.2. Relationship Between ICF and σ_{ext} With Different T

Figure 2a shows the relationship between ICF and σ_{ext} with six T bins using the same data sets as in Figure 1a. The curves of the highest and lowest T bins are flat, denoting that T is quite influential in deciding ICF in these temperature ranges as shown by Yoshida et al. (2010). Compared with the lowest T case, the highest T curve is less flat, particularly around the high σ_{ext} region, due to promotion of the freezing by dust. For the other four T bins, however, the curves increase monotonically with different slopes depending on σ_{ext} values. Especially, the two central curves (248–255 K) are steeper, as illustrated that ICF values were most widely distributed in Figure 1a.

Similar to the case of T, the sensitivity of ICF with regard to σ_{ext} was also investigated. Figure 2b presents $\Delta\ (ICF)/\Delta\sigma_{ext}$, i.e., the slope of curves in Figure 2a, as a function of T for six σ_{ext} bins. All values are positive because ICF is an increasing function of σ_{ext}. All curves were convex, with the peak position shifting toward higher T regions as σ_{ext} increased. We also find the following similar features to the previous subsection: the highest sensitivity at intermediate σ_{ext} and T values; the lowest sensitivity at the highest σ_{ext} and lowest T values, and vice versa (especially at the highest σ_{ext} and lowest T case in this study); the higher sensitivity at smaller σ_{ext} in the lowest T, and vice versa. These features on the sensitivity of ICF could be understood as follows. The sensitivity of ICF takes the lowest both at the largest σ_{ext} and lowest T values where both factors enhance freezing and at the smallest σ_{ext} and highest T values where both factors inhibit freezing, while the sensitivity of ICF gets the highest at the quite distinct situation from the lowest case like intermediate σ_{ext} and T values. Additionally, due to the competing effect of σ_{ext} (the higher, the easier for freezing) and T (the

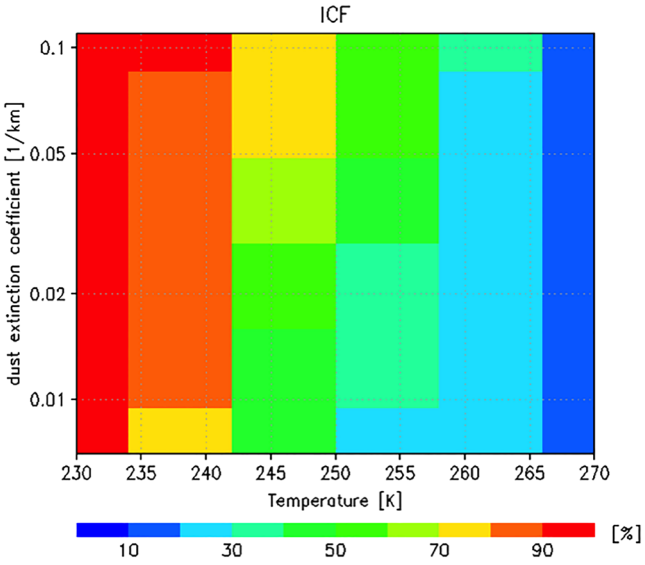

Figure 3. A diagram illustrating ICF with the *x* axis as T and the *y* axis as σ_{ext}.

lower, the easier for freezing), the sensitivity of ICF becomes higher as σ_{ext} gets smaller in the lowest T and as σ_{ext} gets larger in the highest T.

Here let us show a diagram illustration of ICF with the *x* axis as T and the *y* axis as σ_{ext} in Figure 3. Although the content is the same as Figures 1a and 2a, the above-mentioned dependence of ICT on T and σ_{ext} could be visually understood.

Figure 4 presents the sample number of each bin in the same framework as Figure 3. The sample number ranges about from 3,900 to 295,000 over the entire area for the entire period.

As for the error estimation, according to Nishizawa et al. (2011), the estimated retrieval error would be at most 30% for σ_{ext}. For example, this error in σ_{ext} would cause the ICF error of about 3% at the 248 K bin in Figure 2a. Moreover, the ECMWF temperature might not be necessarily the same as the cloud temperature derived from Imaging Infrared Radiometer (IIR) (e.g., Hu et al., 2010), thus further studies are required to examine associated uncertainties more quantitatively, together with the uncertainty from changing the lidar ratio particularly for thick dust cases as mentioned in the section 2.

3.3. Comparison With Previous Studies on ICF Behaviors

These overall tendencies of ICF relative to T and σ_{ext} in this study are consistent with the findings of previous studies, which have shown a positive relationship between ice-containing fraction and the less-quantitative indicator of dustiness (dust frequency, etc.) and a negative relationship between ICF and T. From Figures 1a and 2a, we conclude that ICF is primarily determined by T (approximately from more than 90% to around 10% from the 233 to 269 K bins), but σ_{ext} is also substantially influential in determining ICF particularly at intermediate T range (approximately from 45% to 75% from the 0.007 to 0.110 km^{-1} bins in case of the 248 K bin), which could be interpreted as increased opportunities for freezing with larger σ_{ext}. As stated in section 1, Choi et al. (2010) and Tan et al. (2014) already concluded that dust would affect ICF, but they did not succeed in determining a quantitative link between the dust load and ICF due to the unavailability of physical parameters, such as the extinction coefficient and optical depth. However, Figure 6 of Tan et al. (2014) shows the relationship between the relative aerosol frequency (RAF) and SCF, and this shows three types of slope, i.e., fairly flat, less steep, and steeper lines, respectively, for the −30, −20, and −10°C isotherms for the dust case. RAF is a less-quantitative parameter for use as a proxy of the aerosol load, and it corresponds to σ_{ext} in this study. These lines in their Figure 6 can be interpreted as the frozen sensitivity of dust for different temperatures, an idea that is essentially the same as our findings shown in Figure 2a.

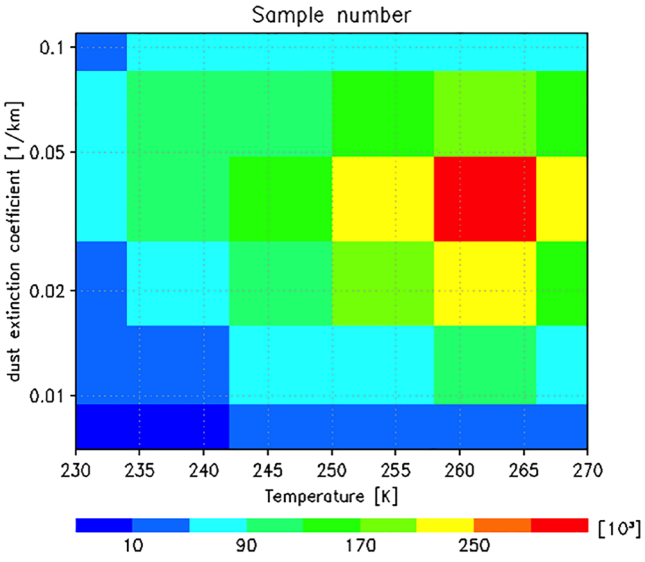

Figure 4. The sample number at each grid of T and σ_{ext} bins. The framework is the same as that of Figure 3.

Also relevant are differences in ice-nucleating ability due to different aerosol species. Tan et al. (2014) considered three types of aerosol (dust, polluted dust, and smoke) and suggested that dust and polluted dust act as INP over some regions, not mentioning smoke in this regard. Gibbs et al. (2015) showed that fine glassy silicic volcanic ash particles from the Santorini Volcano in Greece enhanced the freezing fraction, but not to the same extent as feldspar dust did. Furthermore, Seifert et al. (2015) found ice-containing clouds 1.5 to 2 times more frequently during the dry season through a seasonal analysis with polarization lidar measurements from Manaus, Brazil (2.3°S, 60°W). Biomass burning was suggested as the possible origin of this phenomenon, as it strongly influenced the aerosol composition during the season, injecting biological material, soil dust, and

ash particles into the atmosphere. Filioglou et al. (2019) also addressed the effect of aerosol type (classified as marine, continental, dust, and elevated smoke) and aerosol load on the cloud phase (water, mixed-phase, and ice) of Arctic low-level clouds. Although they introduced a quantitative parameter, aerosol optical depth, to estimate the role of the aerosol load on freezing, their discussion was limited to two categories: high and low aerosol optical depths.

As defined earlier, ICF is also dependent on the sample number of liquid water. Thus, ICF is also influenced by updraft velocity and supersaturation (e.g., Hill et al., 2014). Moreover, ice crystals are formed also due to incorporating INP by the cloud top entrainment (Fridlind et al., 2012). Recently, Coopman et al. (2020) found that cloud glaciation temperature, defined as the temperature for which the ICF is equal to 50%, decreased with stronger vertical pressure velocity at 700 hPa. In this regard, further research would be required considering the effects of meteorology and cloud thermodynamics to better understand ICF behaviors.

4. Conclusions

Using 3-year data for the thermodynamic phase of the cloud top and σ_{ext} derived from CALIPSO data, this study examined the effects of σ_{ext} on cloud phase partitioning by comparing these two parameters with spatial proximity over latitudes greater than 45° in the Northern Hemisphere. This study has the advantage of using a quantitative physical parameter of the extinction coefficient as the dust load indicator, rather than merely the aerosol type information, as it can be converted into less-quantitative parameters, such as the relative frequency. Our findings are summarized as follows.

1. From Figure 1a, ICF was a monotonic function of T for all ranges of σ_{ext}. Flatter and steeper parts could be observed near the lowest and highest T, and intermediate T bins, respectively, indicating convex in lower T and concave shapes in higher T ranges. The larger σ_{ext} was, the larger ICF became in the same T bin, and vice versa. Although the variation in ICF due to differences in σ_{ext} in the same T bin was smaller in the bins near the low and high ends, those in the intermediate T bins were larger. In particular, ICF values were most spread around the intermediate T bins (248–255 K), with an almost 30% difference maximum.
2. From Figure 2a, the curves of the highest and lowest T bins were quite flat in relation to σ_{ext}. Compared with the lowest T, the highest T curve was less flat near the high σ_{ext} regions, due to promotion of the freezing by dust. For the other intermediate T bins, however, the curves increased monotonically with different slopes depending on σ_{ext} values. Especially, the central two curves (248–255 K) were steeper corresponding to the greatest spread of ICF values in Figure 1a.
3. From the above analyses thus obtained, we concluded that ICF was primarily determined by T, but σ_{ext} was also substantially influential in determining ICF particularly in intermediate T range, which could be interpreted as increased opportunities for freezing with larger σ_{ext}. As for the sensitivity of ICF from Figures 1b and 2b, it took the lowest both at the largest σ_{ext} and lowest T values and at the smallest σ_{ext} and highest T values, while it got the highest at intermediate σ_{ext} and T values. Also, the sensitivity of ICF became higher as σ_{ext} got smaller in the lowest T and as σ_{ext} got larger in the highest T. These behaviors could be understood from the combination of specific characteristics of T (the lower, the easier for freezing) and σ_{ext} (the larger, the easier for freezing).

As stated in section 2, we evaluated the cloud top phase using σ_{ext} values just above the cloud top, assuming the incorporation of INPs through cloud top entrainment. Comparisons of the cloud base phase with σ_{ext} values just below the cloud base are generally desirable, since clouds usually form via updrafts. However, this analysis is difficult to perform due to strong attenuation of satellite lidar signals, but the ground-based lidars would more clearly demonstrate the influence of dust particles from the ground, where they are significantly more abundant.

Finally, this study addressed the only dust property of the extinction coefficient, but other microphysical properties (e.g., the number concentration and size distribution) would be interesting to consider. The relationship between the number concentrations of ice and dust particles is also of great interest. Ice number concentration is determined using the effective radius, ice water content, mixing ratio of the 2-D plate with 3-D ice categories by using attenuated backscattering coefficient and depolarization ratio at 532 nm from

CALIPSO and radar reflectivity factor from CloudSat (Okamoto et al., 2010; Sato & Okamoto, 2011; Sourdeval et al., 2018). Thus, it is straightforward to study the relation. Space-borne Doppler cloud profiling radar (CPR) and high-spectral-resolution atmospheric lidar (ATLID) will be onboard on the EarthCARE satellite in 2022. The lidar ratio information is expected from ATLID so that more reliable ice particle classification will be possible through analyses of 2-D diagram of lidar ratio and depolarization ratio at 355 nm (Okamoto et al., 2019).

Acknowledgments
We thank the editor and two anonymous reviewers for constructive comments on our manuscript. The cloud and aerosol products that were used in this paper were supplied by the EarthCARE Research Product Monitor (www.eorc.jaxa.jp/EARTHCARE/research_product/ecare_monitor.html), Japan Aerospace Exploration Agency (JAXA). This work was supported by JSPS KAKENHI grant JP16H02942, JP16H04046, JP17H06139, by the JAXA EarthCARE project and by General Research 2019-A025, RIAM, Kyushu University. Dr. N. Orikasa of MRI, JMA and Dr. T. Nishizawa of NIES gave us useful comments to interpret the phenomena.

References

Bodas-Salcedo, A., Hill, P. G., Furtado, K., Williams, K. D., Field, P. R., Manners, J. C., et al. (2016). Large contribution of supercooled liquid clouds to the solar radiation budget of the Southern Ocean. *Journal of Climate*, *29*, 4213–4228. https://doi.org/10.1175/JCLI-D-15-0564.1

Burrows, S. M., Hoose, C., Pöschl, U., & Lawrence, M. G. (2013). Ice nuclei in marine air: Biogenic particles or dust? *Atmospheric Chemistry and Physics*, *13*, 245–267. https://doi.org/10.5194/acp-13-245-2013

Choi, Y.-S., Lindzen, R. S., Ho, C.-H., & Kim, J. (2010). Space observations of cold-cloud phase change. *Proceedings of the National Academy of Sciences*, *107*(25), 11211–11216. https://doi.org/10.1073/pnas.1006241107

Coopman, Q., Riedi, J., Zeng, S., & Garrett, T. J. (2020). Space based analysis of the cloud thermodynamic phase transition for varying microphysical and meteorological regimes. *Geophysical Research Letters*, *47*, e2020GL087122. https://doi.org/10.1029/2020GL087122

Dubovik, O., Sinyuk, A., Lapyonok, T., Holben, B. N., Mishchenko, M. I., Yang, P., et al. (2006). Application of spheroid models to account for aerosol particle nonsphericity in remote sensing of desert dust. *Journal of Geophysical Research*, *111*, D11208. https://doi.org/10.1029/2005JD006619

Filioglou, M., Mielonen, T., Balis, D., Giannakaki, E., Arola, A., Kokkola, H., et al. (2019). Aerosol effect on the cloud phase of low-level clouds over the Arctic. *Journal of Geophysical Research: Atmospheres*, *124*, 7886–7899. https://doi.org/10.1029/2018JD030088

Fridlind, A. M., van Diedenhoven, B., Ackerman, A. S., Avramov, A., Mrowiec, A., Morrison, H., et al. (2012). A FIRE-ACE/SHEBA case study of mixed-phase Arctic boundary layer clouds: Entrainment rate limitations on rapid primary ice nucleation processes. *Journal of the Atmospheric Sciences*, *69*, 365–389. https://doi.org/10.1175/JAS-D-11-052.1

Fu, Q., & Liou, K. N. (1993). Parameterization of the radiative properties of cirrus clouds. *Journal of the Atmospheric Sciences*, *50*(13), 2008–2025. https://doi.org/10.1175/1520-0469(1993)050<2008:POTRPO>2.0.CO;2

Gibbs, A., Charman, M., Schwarzacher, W., & Rust, A. C. (2015). Immersion freezing of supercooled water drops containing glassy volcanic ash particles. *GeoResJ*, *7*, 66–69. https://doi.org/10.1016/j.grj.2015.06.002

Hagihara, Y., Okamoto, H., & Yoshida, R. (2010). Development of a combined CloudSat/CALIPSO cloud mask to show global cloud distribution. *Journal of Geophysical Research*, *115*, D00H32. https://doi.org/10.1029/2009JD012344

Hill, A. A., Field, P. R., Furtado, K., Korolev, A., & Shipway, B. J. (2014). Mixed-phase clouds in a turbulent environment. Part 1: Large-eddy simulation experiments. *Quarterly Journal of the Royal Meteorological Society*, *140*, 855–869. https://doi.org/10.1002/qj.2177

Hirakata, M., Okamoto, H., Hagihara, Y., Hayasaka, T., & Oki, R. (2014). Comparison of global and seasonal characteristics of cloud phase and horizontal ice plates derived from CALIPSO with MODIS and ECMWF. *Journal of Atmospheric and Oceanic Technology*, *31*(10), 2114–2130. https://doi.org/10.1175/JTECH-D-13-00245.1

Hoose, C., & Möhler, O. (2012). Heterogeneous ice nucleation on atmospheric aerosols: A review of results from laboratory experiments. *Atmospheric Chemistry and Physics*, *12*, 9817–9854. https://doi.org/10.5194/acp-12-9817-2012

Hu, Y., Winker, D., Vaughan, M., Lin, B., Omar, A., Trepte, C., et al. (2009). CALIPSO/CALIOP cloud phase discrimination algorithm. *Journal of Atmospheric and Oceanic Technology*, *26*, 2293–2309. https://doi.org/10.1175/2009JTECHA1280.1

Hu, Y. X., Rodier, S., Xu, K. M., Sun, W. B., Huang, J. P., Lin, B., et al. (2010). Occurrence, liquid water content, and fraction of supercooled water clouds from combined CALIOP/IIR/MODIS measurements. *Journal of Geophysical Research*, *115*, D00H34. https://doi.org/10.1029/2009JD012384

Isono, K., Komabayashi, M., & Ono, A. (1959). The nature and the origin of ice nuclei in the atmosphere. *Journal of the Meteorological Society of Japan*, *37*(6), 211–233. https://doi.org/10.2151/jmsj1923.37.6_211

Kanitz, T., Seifert, P., Ansmann, A., Engelmann, R., Althausen, D., Casiccia, C., & Rohwer, E. G. (2011). Contrasting the impact of aerosols at northern and southern midlatitudes on heterogeneous ice formation. *Geophysical Research Letters*, *38*, L17802. https://doi.org/10.1029/2011GL048532

Komurcu, M., Storelvmo, T., Tan, I., Lohmann, U., Yun, Y., Penner, J. E., et al. (2014). Intercomparison of the cloud water phase among global climate models. *Journal of Geophysical Research: Atmospheres*, *119*, 3372–3400. https://doi.org/10.1002/2013JD021119

Manabe, S., & Wetherald, R. T. (1975). The effect of doubling the CO_2 concentration on the climate of a general circulation model. *Journal of the Atmospheric Sciences*, *32*(1), 3–15. https://doi.org/10.1175/1520-0469(1975)032<0003:TEODTC>2.0.CO;2

McCoy, D. T., Hartmann, D. L., Zelinka, M. D., Ceppi, P., & Grosvenor, D. P. (2015). Mixed-phase cloud physics and Southern Ocean cloud feedback in climate models. *Journal of Geophysical Research: Atmospheres*, *120*, 9539–9554. https://doi.org/10.1002/2015JD023603

Müller, D., Ansmann, A., Mattis, I., Tesche, M., Wandinger, U., Althausen, D., & Pisani, G. (2007). Aerosol-type-dependent lidar ratios observed with Raman lidar. *Journal of Geophysical Research*, *112*, D16202. https://doi.org/10.1029/2006JD008292

Murray, B. J., O'Sullivan, D., Atkinson, J. D., & Webb, M. E. (2012). Ice nucleation by particles immersed in supercooled cloud droplets. *Chemical Society Reviews*, *41*(19), 6519–6554. https://doi.org/10.1039/C2CS35200A

Nishizawa, T., Okamoto, H., Sugimoto, N., Matsui, I., Shimizu, A., & Aoki, K. (2007). An algorithm that retrieves aerosol properties from dual-wavelength polarization lidar measurements. *Journal of Geophysical Research*, *112*, D06212. https://doi.org/10.1029/2006JD007435

Nishizawa, T., Okamoto, H., Takemura, T., Sugimoto, N., Matsui, I., & Shimizu, A. (2008). Aerosol retrieval from two-wavelength backscatter and one-wavelength polarization lidar measurement taken during the MR01K02 cruise of the R/V Mirai and evaluation of a global aerosol transport model. *Journal of Geophysical Research*, *113*, D21201. https://doi.org/10.1029/2007JD009640

Nishizawa, T., Sugimoto, N., Matsui, I., Shimizu, A., & Okamoto, H. (2011). Algorithms to retrieve optical properties of three component aerosols from two-wavelength backscatter and one-wavelength polarization lidar measurements considering nonsphericity of dust. *Journal of Quantitative Spectroscopy & Radiative Transfer*, *112*, 254–267. https://doi.org/10.1016/j.jqsrt.2010.06.002

Okamoto, H., Nishizawa, T., Takemura, T., Kumagai, H., Kuroiwa, H., Sugimoto, N., et al. (2007). Vertical cloud structure observed from ship-borne radar and lidar: Mid-latitude case study during the MR01/K02 cruise of the research vessel Mirai. *Journal of Geophysical Research*, *112*, D08216. https://doi.org/10.1029/2006JD007628

Okamoto, H., Nishizawa, T., Takemura, T., Sato, K., Kumagai, H., Ohno, Y., et al. (2008). Vertical cloud properties in the tropical western Pacific Ocean: Validation of the CCSR/NIES/FRCGC GCM by shipborne radar and lidar. *Journal of Geophysical Research*, *113*, D24213. https://doi.org/10.1029/2008JD009812

Okamoto, H., Sato, K., Borovoi, A., Ishimoto, H., Masuda, K., Konoshonkin, A., & Kustova, N. (2019). Interpretation of lidar ratio and depolarization ratio of ice clouds using spaceborne high-spectral-resolution polarization lidar. *Optics Express*, *27*(25), 36,587–36,600. https://doi.org/10.1364/OE.27.036587

Okamoto, H., Sato, K., & Hagihara, Y. (2010). Global analysis of ice microphysics from CloudSat and CALIPSO: Incorporation of specular reflection in lidar signals. *Journal of Geophysical Research*, *115*, D22209. https://doi.org/10.1029/2009JD013383

Partain, P. (2007). Cloudsat ECMWF-AUX auxiliary data process description and interface control document, report, 10 pp., CloudSat Proj., Colo. State Univ., Fort Collins.

Pratt, K. A., DeMott, P. J., French, J. R., Wang, Z., Westphal, D. L., Heymsfield, A. J., et al. (2009). In situ detection of biological particles in cloud ice-crystals. *Nature Geoscience*, *2*(6), 398–401. https://doi.org/10.1038/ngeo521

Pruppacher, H. R., & Klett, J. D. (1978). *Microphysics of Clouds and Precipitation* (pp. 1–954). New York, NY: Springer. https://doi.org/10.1007/978-0-306-48100-0

Sassen, K., DeMott, P. J., Prospero, J. M., & Poellot, M. R. (2003). Saharan dust storms and indirect aerosol effects on clouds: CRYSTAL-FACE results. *Geophysical Research Letters*, *30*(12), 1633. https://doi.org/10.1029/2003GL017371

Sato, K., & Okamoto, H. (2011). Refinement of global ice microphysics using spaceborne active sensors. *Journal of Geophysical Research*, *116*, D20202. https://doi.org/10.1029/2011JD015885

Sato, K., Okamoto, H., & Ishimoto, H. (2018). Physical model for multiple scattered space-borne lidar returns from clouds. *Optics Express*, *26*, A301–A319. https://doi.org/10.1364/OE.26.00A301

Sato, K., Okamoto, H., & Ishimoto, H. (2019). Modeling the depolarization of space-borne lidar signals. *Optics Express*, *27*(4), A117–A132. https://doi.org/10.1364/OE.27.00A117

Screen, J. A., & Simmonds, I. (2010). The central role of diminishing sea ice in recent Arctic temperature amplification. *Nature*, *464*(7293), 1334–1337. https://doi.org/10.1038/nature09051

Seifert, P., Kunz, C., Baars, H., Ansmann, A., Bühl, J., Senf, F., et al. (2015). Seasonal variability of heterogeneous ice formation in stratiform clouds over the Amazon Basin. *Geophysical Research Letters*, *42*, 5587–5593. https://doi.org/10.1002/2015GL064068

Shupe, M. D., Daniel, J. S., De Boer, G., Eloranta, E. W., Kollias, P., Long, C. N., et al. (2008). A focus on mixed-phase clouds: The status of ground-based observational methods. *Bulletin of the American Meteorological Society*, *89*, 1549–1562. https://doi.org/10.1175/2008BAMS2378.1

Slingo, A. (1989). A GCM parameterization for the shortwave radiative properties of clouds. *Journal of the Atmospheric Sciences*, *46*(10), 1419–1427. https://doi.org/10.1175/1520-0469(1989)046<1419:AGPFTS>2.0.CO;2

Sourdeval, O., Gryspeerdt, E., Krämer, M., Goren, T., Delanoë, J., Afchine, A., et al. (2018). Ice crystal number concentration estimates from lidar–radar satellite remote sensing—Part 1: Method and evaluation. *Atmospheric Chemistry and Physics*, *18*, 14327–14350. https://doi.org/10.5194/acp-18-14327-2018

Tan, I., & Storelvmo, T. (2019). Evidence of strong contributions from mixed-phase clouds to Arctic climate change. *Geophysical Research Letters*, *46*, 2894–2902. https://doi.org/10.1029/2018GL081871

Tan, I., Storelvmo, T., & Choi, Y.-S. (2014). Spaceborne lidar observations of the ice-nucleating potential of dust, polluted dust, and smoke aerosols in mixed-phase clouds. *Journal of Geophysical Research: Atmospheres*, *119*, 6653–6665. https://doi.org/10.1002/2013JD021333

Taylor, P. C., Cai, M., Hu, A., & Meehl, J. (2013). A decomposition of the feedback contributions to polar warming amplification. *Journal of Climate*, *26*, 7023–7043. https://doi.org/10.1175/JCLI-D-12-00696.1

Tobo, Y., Adachi, K., DeMott, P. J., Hill, T. C. J., Hamilton, D. S., Mahowald, N. M., et al. (2019). Glacially sourced dust as a potentially significant source of ice nucleating particles. *Nature Geoscience*, *12*(4), 253–258. https://doi.org/10.1038/s41561-019-0314-x

Wandinger, U., Tesche, M., Seifert, P., Ansmann, A., Müller, D., & Althausen, D. (2010). Size matters: Influence of multiple scattering on CALIPSO light-extinction profiling in desert dust. *Geophysical Research Letters*, *37*, L10801. https://doi.org/10.1029/2010GL042815

Wilson, T. W., Ladino, L. A., Alpert, P. A., Breckels, M. N., & Brooks, I. M. (2015). A marine biogenic source of atmospheric ice-nucleating particles. *Nature*, *525*, 234–238. https://doi.org/10.1038/nature14986

Yoshida, Y., Okamoto, H., & Hagihara, Y. (2010). Global analysis of cloud phase and ice crystal orientation from Cloud–Aerosol Lidar and Infrared Pathfinder Satellite Observation (CALIPSO) data using attenuated backscattering and depolarization. *Journal of Geophysical Research*, *115*, D00H32. https://doi.org/10.1029/2009JD012334

Zhang, D., Liu, D., Luo, T., Wang, Z., & Yin, Y. (2015). Aerosol impacts on cloud thermodynamic phase change over East Asia observed with CALIPSO and CloudSat measurements. *Journal of Geophysical Research: Atmospheres*, *120*, 1490–1501. https://doi.org/10.1002/2014JD022630

Zhao, B., Gu, Y., Liou, K.-N., Wang, Y., Liu, X., Huang, L., et al. (2018). Type-dependent responses of ice cloud properties to aerosols from satellite retrievals. *Geophysical Research Letters*, *45*, 3297–3306. https://doi.org/10.1002/2018GL077261